Progress In Electromagnetics Research B, Vol. 7, 223–244, 2008

SOME FAR FIELD FEATURES OF CYLINDRICAL MICROSTRIP ANTENNA ON AN ELECTRICALLY SMALL CYLINDER

A. Y. Svezhentsev

The A.Ya. Usikov Institute of Radio Physics and Electronics
The National Academy of Sciences of Ukraine
12, Akad. Proskury Str., 61085, Kharkov, Ukraine

Abstract—The far field behavior of a small wave size cylindrical microstrip antenna (CMA) has been originally analyzed for a small elevation angle, where a pronounced maximum has been found. Also it has been found that a similar maximum takes place in the far field of an electric dipole taken instead of the patch. It has been shown that the phenomenon originates to the far field behavior of the annular electric current given in the form of $n = 1$ azimuthally traveling wave harmonic held in the series representation of the electric dipole field. Approximate analytical expressions have been obtained describing the far-field components for two different polarizations. Also, the CMA radiation pattern is shown to bear similarities to the pattern of an electric dipole placed on a dielectric substrate surrounding a circular metal cylinder.

1. INTRODUCTION

Cylindrical microstrip antennas (CMA) (see Fig. 1) have been gaining acceptance in space and mobile communications. The CMA theory is based on studies of the scattering from infinite metal or dielectric-coated metal cylinders, the structure excitation by elementary sources and the radiation from the patches placed at the interfaces in a stratified dielectric medium around the metal cylinder [1–23]. As the theoretical analysis enhanced and grew more rigorous, approximate CMA simulations [12, 13] gave way to more accurate models [14–17]. In particular, the CMA far field and the impedance have been calculated by the method of moments in the spectral domain [17]. On the whole, the above-mentioned CMA models work well for electrically

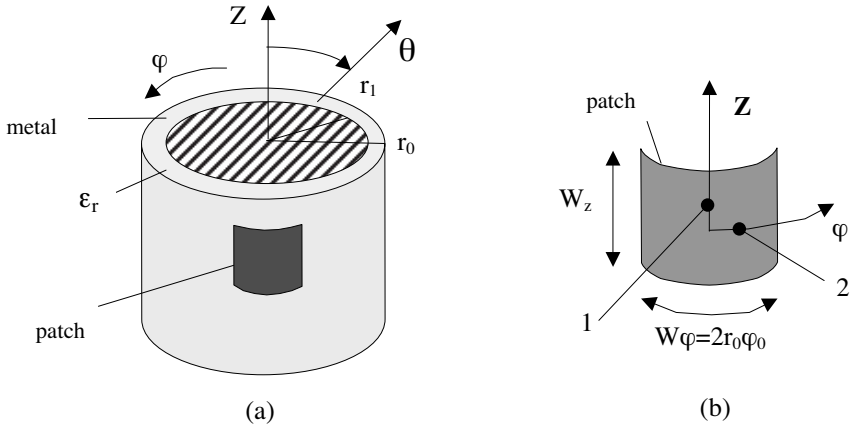

Figure 1. (a) cylindrical microstrip antenna and (b) patch geometry. Numbers 1 and 2 mark different probe positions on the patch and correspond to the z-polarized patch case (1) and the φ-polarized patch case (2).

small antennas, the metal cylinder radius smaller than the wavelength ($r_1 < \lambda_0$).

The CMA theory enhancement goes through the development of new approaches [18–20] in an effort to deal with any electric size of the antenna and any shape of the patches, including electrically large antennas with the cylinder radius quite exceeding the wavelength [20] and multilayer antennas, among them antenna arrays [21].

The major CMA criterion is the far field behavior. But even though nearly every CMA study comes with far-field simulations (see the references above), there are still some far-field essentials escaping our awareness.

The present paper will discuss the far field features that a small wave size CMA displays at a small elevation. In this case, the CMA far field components are found to have a local maximum. The situation becomes clear by considering the electric dipole problem and the annular electric current case of $n = 1$ azimuthally traveling wave harmonic. A far-field comparative analysis will be made between the CMA and the electric dipole placed on a dielectric substrate surrounding a circular metal cylinder. The instrument will be some recent approach [18] based on the method of moments in the space domain using proper Green's functions [22, 23].

2. CMA PROBLEM FORMULATION AND FAR FIELD EVALUATION

The CMA from Fig. 1 represents a rectangular cylindrical metal patch placed on the so-called Goubau line [24] in the form of a z-infinite circular metal cylinder of radius r_1 surrounded by a circular dielectric substrate of radius r_0 and related permittivity ε_r.

The emphasis will be on the far field behavior rather than the problem solution. The resonant frequency current distribution on the patch is assumed to be known. The present study bears general character, with the solution technique of no concern. For definiteness sake, the patch current distribution is as that from [18, 22, 23].

The z-components of the electric and magnetic field in the spectral domain are [17, 23]

$$e_{zn}(r,h) = \chi^E_{zzn}(r,h)j_z(h) + \chi^E_{z\varphi n}(r,h)j_\varphi(h); \tag{1}$$

$$h_{zn}(r,h) = \chi^H_{zzn}(r,h)j_z(h) + \chi^H_{z\varphi n}(r,h)j_\varphi(h), \tag{2}$$

where $e_{zn}(r,h)$ and $h_{zn}(r,h)$ are the z-components of the electric and magnetic fields in the spectral domain, $\chi^{E,H}_{pqn}(r,h)$ are the components of Green's spectral function, p and q stand for z or φ, and $j_z(h)$ and $j_\varphi(h)$ are the spectral components of the patch surface current. For the spectral Green's functions $\chi^{E,H}_{pqn}(r,h)$, see Appendix A. The space domain transformation of (1)–(2) gives

$$\begin{bmatrix} E_z(r,\varphi,z) \\ H_z(r,\varphi,z) \end{bmatrix} = \int\limits_{z'}\int\limits_{\varphi'} \begin{bmatrix} J^e_z(\varphi',z') \\ J^e_\varphi(\varphi',z') \end{bmatrix} \hat{G}(r,z,z',\varphi,\varphi') \cdot dz'd\varphi' \tag{3}$$

where $\hat{G} = \begin{bmatrix} \hat{G}^E_{z\,z} & \hat{G}^E_{z\,\varphi} \\ \hat{G}^H_{z\,z} & \hat{G}^H_{z\,\varphi} \end{bmatrix}$,

$$G^{E,H}_{p\,q}(r,\varphi-\varphi',z-z') = \frac{1}{4\pi^2}\sum_{n=-\infty}^{\infty} e^{-in(\varphi-\varphi')} \int\limits_{h=-\infty}^{\infty} \chi^{E,H}_{pqn}(r,h)e^{-ih(z-z')}dh, \tag{4}$$

and $G^{E,H}_{p\,q}(r,\varphi-\varphi',z-z')$ is the spatial Green's function component, which is the spatial equivalent of $\chi^{E,H}_{pqn}(r,h)$ function. The far zone

translation readily follows after rewriting (3) as

$$\begin{bmatrix} E_z(r,\varphi,z) \\ H_z(r,\varphi,z) \end{bmatrix} = \int\limits_{z'}\int\limits_{\varphi'} \begin{bmatrix} J_z^e(\varphi',z') \\ J_\varphi^e(\varphi',z') \end{bmatrix} \left[\frac{1}{4\pi^2} \sum_{n=-\infty}^{\infty} e^{-in(\varphi-\varphi')} \hat{\Psi}_n(r,z) \right] dz' d\varphi'. \tag{5}$$

Here $\hat{\Psi}_n(r,z) = \begin{bmatrix} \Psi_{zzn}^E(r,z) & \Psi_{z\varphi n}^E(r,z) \\ \Psi_{zzn}^H(r,z) & \Psi_{z\varphi n}^H(r,z) \end{bmatrix}$,

$$\Psi_{pqn}^{E,H}(r,z) = \int\limits_{-\infty}^{\infty} \bar{\chi}_{pqn}^{E,H}(h) \left[H_n^{(2)}\left(r\tilde{k}_0\right) / H_n^{(2)}(x_0) \right] e^{-ih(z-z')} dh, \tag{5a}$$

$k_0 = 2\pi/\lambda_0$, where λ_0 is the free space wavelength. For $\tilde{k}_0$ and x_0, refer to Appendix.

Spectral functions $\chi_{p\,q\,n}^{E,H}(r,h)$ and $\bar{\chi}_{p\,q\,n}^{E,H}(h)$ relate as

$$\chi_{p\,q\,n}^{E,H}(r,h) = \bar{\chi}_{p\,q\,n}^{E,H}(h) \left[H_n^{(2)}\left(r\tilde{k}_0\right) / H_n^{(2)}(x_0) \right]. \tag{6}$$

The asymptotical representation of Fourier integral (5a) yields [25]

$$\Psi_{p\,q\,n}^{E,H}(R,\theta) \to -2\frac{e^{-ik_0R}}{R} i^{n+1} e^{iz'k_0\cos(\theta)} \chi_{pqn}^{E,H}(k_0\cos(\theta)). \tag{7}$$

Finally the far filed is

$$\begin{bmatrix} E_z(R,\varphi,\theta) \\ H_z(R,\varphi,\theta) \end{bmatrix} = -2\frac{e^{-ik_0R}}{R} \frac{1}{4\pi^2} \sum_{n=-\infty}^{\infty} e^{-in\varphi} i^{n+1} \begin{bmatrix} j_{nz}^e(\theta) \\ j_{n\varphi}^e(\theta) \end{bmatrix} \hat{\chi}(\theta), \tag{8}$$

$$\hat{\chi}(\theta) = \begin{bmatrix} \chi_{zzn}^E(k_0\cos(\theta)) & \chi_{z\varphi n}^E(k_0\cos(\theta)) \\ \chi_{zzn}^H(k_0\cos(\theta)) & \chi_{z\varphi n}^H(k_0\cos(\theta)) \end{bmatrix},$$

$$j_{n\,s}^e(\theta) = \int\limits_{z'}\int\limits_{\varphi'} J_s^e\left(\varphi',z'\right) e^{in\varphi'} e^{ik_0\cos(\theta)z'} d\varphi' dz'. \tag{9}$$

Now that the E_z- and H_z-components of the far field in cylindrical coordinates are known, the transverse components of the spherical wave field in the far zone are [25]

$$E_\theta = -\frac{E_z}{\sin\theta} \quad \text{and} \quad E_\varphi = \frac{w_0 H_z}{\sin\theta}, \tag{10}$$

where w_0 is the free space wave impedance.

3. SMALL-θ CHARACTERISTIC FEATURES OF THE CMA CO-POLAR PATTERN IN THE E-PLANE (z-POLARIZED PATCH) AND IN THE H-PLANE (φ-POLARIZED PATCH)

The CMA metal patch (Fig. 1) is assumed to be of the size $W_z = 0.08\,\mathrm{m}$ and $W_\varphi = 0.0854\,\mathrm{m}$. The patch lies on a dielectric substrate having related permittivity $\varepsilon_r = 2.3$ and placed on a metal cylinder of radius $r_1 = 0.1\,\mathrm{m}$. The radius relationship of the dielectric substrate and the metal cylinder is $r_0/r_1 = 1.02$, which is equivalent to a $d = 2\,\mathrm{mm}$ thick dielectric substrate.

The CMA radiation patterns will be considered for two polarizations. The z-polarized patch produces θ-polarization (which is principal one here) of the CMA radiation pattern. In this case the patch is probe-fed at the point $z_p = 0.02\,\mathrm{m}$, $\varphi_p = 0$. The φ-polarized patch gives φ-polarization (the principal one) of the CMA radiation pattern. The feeding point is $z_p = 0$, $r_0\varphi_p = 0.021\,\mathrm{m}$. The CMA parameters are as those in [17].

The co-polar pattern in the E-plane (E_θ versus θ) for the z-polarized patch and the co-polar pattern in the H-plane (E_φ versus θ) for the φ-polarized patch are shown in Fig. 2 at resonant frequency $f_0 = 1.2\,\mathrm{GHz}$ The calculations were made, as mentioned, by the method described in [18, 22, 23]. The curves fully agree with the results from [14] and [17]. However neither in [14, 17] nor anywhere else, the $E_\theta(\theta)$ and $E_\varphi(\theta)$ components were examined for a small θ. Specifically, Fig. 2 and the data from [14, 17] show that the electric field components increase at a small θ, whereas from [19, Fig. 6] it follows that those field components approach some constant as θ vanishes. This sends us in research of the point.

3.1. The Co-Polar Pattern in the E-Plane for z-polarized Patch

Let us begin with the co-polar pattern in the E-plane for the z-polarized patch (E_θ versus θ, the triangles in Fig. 2). Of interest is the E_θ far field in the plane $\varphi = 0°$, with only the z-component of the electric current contributing to the far field. With (8), the zth electric field component in the far zone becomes

$$E_z(R, \varphi = 0, \theta) = \\ -2\frac{e^{-ik_0R}}{R}\frac{1}{4\pi^2}\sum_{n=-\infty}^{\infty} i^{n+1}\left[\bar{\chi}^E_{zzn}(k_0\cos(\theta))/H_n^{(2)}(k_0r_0\sin(\theta))\right] j^e_{nz}(\theta). \tag{11}$$

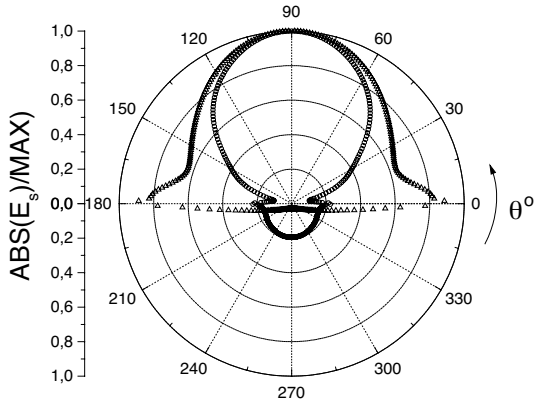

Figure 2. The co-polar pattern in the E-plane (E_θ versus θ) for the z-polarized patch (triangles) and the co-polar pattern in the H-plane (E_φ versus θ) for the φ-polarized patch (circles), the θ step is 1°.

In view of the excitation symmetry, the summation in (11) can be reduced to that from 0 to $\propto$. So,

$$E_z(R,\varphi=0,\theta)= \\ -2\frac{e^{-i\,k_0\,R}}{R}\frac{1}{4\pi^2}\sum_{n=0}^{\infty}\alpha_n i^{n+1}\left[\bar{\chi}^E_{zzn}(k_0\cos(\theta))/H_n^{(2)}(k_0 r_0\sin(\theta))\right]j^e_{nz}(\theta), \tag{12}$$

$$\alpha_n=\begin{cases}1 & n=0,\\ 2 & n>0.\end{cases}$$

In the derivation of (12), care was taken of that

$$\bar{\chi}^E_{zz,-n}(k_0\cos(\theta))/H^{(2)}_{-n}(k_0 r_0\sin(\theta))= \\ (-1)^n\bar{\chi}^E_{zz,n}(k_0\cos(\theta))/H_n^{(2)}(k_0 r_0\sin(\theta)), \tag{13}$$

and, also, the current principal mode distribution in the θ-polarization case obeys the rule

$$j^e_{-n,z}(\theta)=\ j^e_{n,z}(\theta). \tag{14}$$

It is found that the $n=1$ harmonic of the Fourier series (12) is the main contributor to the far $E_\theta(\theta)$ field at $\varphi=0$ and θ small. Hence

for small θ angles, (12) reduces rather accurately to

$$E_z(R,\varphi\ =\ 0,\theta) \cong \frac{-1}{2\pi^2}\frac{2\,e^{-i\,k_0\,R}}{R} \left[\bar{\chi}^E_{z\,z,\,1}(k_0\,\cos(\theta))/H_1^{(2)}(k_0 r_0\,\sin(\theta))\right] j^e_{1,z}(\theta). \quad (15)$$

Consider how the spectral function $\bar{\chi}^E_{zz,1}(k_0\cos(\theta))/H_1^{(2)}(k_0 r_0\sin(\theta))$ in the square brackets in (15) behaves at a small θ. With the cylindrical function small-argument approximation [26], the spectral function approximates to

$$\bar{\chi}^E_{zz,+1}(k_0\cos(\theta))/H_1^{(2)}(k_0 r_0\sin(\theta)) \cong -\frac{\pi k_0 r_0 \sin(\theta)}{2k_0 r_0\left\{2\ln\left[\gamma k_0 r_0 \sin(\theta)x/2\right] + i(\pi - \varepsilon_r B)\right\}}, \quad (16)$$

where B is a purely imaginary constant dependent on frequency, geometrical and constitutive parameters of the structure; it is evaluated via the cylindrical function combination at the branch point (see Appendix).

Expressed via $E_z(R,\varphi=0,\theta)$ in view of (10), the field component $E_\theta(R,\varphi=0,\theta)$ becomes

$$E_\theta(R,\varphi=0,\theta) \cong \frac{1}{4\pi^2}\frac{e^{-ik_0R}}{R}\frac{2\pi}{\left[2\ln\left[\gamma k_0 r_0\sin(\theta)/2\right] + i(\pi - B)\right]} j^e_{1,z}(\theta). \quad (17)$$

3.2. The Co-Polar Pattern in the H-Plane for the φ-Polarization Patch

Take up the co-polar pattern in the H-plane for the φ-polarized patch (E_φ versus θ, the circles in Fig. 2). The far E_φ component in the $\varphi = 0^\circ$ plane can be calculated via H_z using (10). The same as the E_z component, H_z comes from (9) as

$$H_z(R,\varphi=0,\theta) = -2\frac{e^{-ik_0R}}{R}\frac{1}{4\pi^2}\sum_{n=0}^{\infty}\alpha_n i^{n+1}\left[\bar{\chi}^H_{zzn}(k_0\cos(\theta))/H_n^{(2)}(k_0 r_0\sin(\theta))\right] j^e_{n\varphi}(\theta). \quad (18)$$

Expression (18) was obtained with regard for

$$\bar{\chi}^H_{zz,-n}(k_0\cos(\theta))/H_{-n}^{(2)}(k_0 r_0\sin(\theta)) = (-1)^n\bar{\chi}^H_{zz,-n}(k_0\cos(\theta))/H_n^{(2)}(k_0 r_0\sin(\theta)), \quad (19)$$

and, also, the current principal mode in φ-polarization obeys the rule

$$j^e_{-n,\varphi}(\theta) = j^e_{n,\varphi}(\theta). \tag{20}$$

The main contributor at a small θ is, as before, the $n = 1$ harmonic of Fourier series (18). Hence, at a small θ, it is suffice to retain the $n = 1$ harmonic alone in (18). With this approximation and the small-argument asymptotic representation of the cylindrical functions,

$$H_z(R, \varphi = 0, \theta) \cong \\ \frac{-1}{2\pi^2}\frac{2e^{-ik_0R}}{R}\left[\bar{\chi}^H_{zz,1}(k_0\cos(\theta))/H^{(2)}_1(k_0r_0\sin(\theta))\right] j^e_{1,\varphi}(\theta), \tag{21}$$

with

$$\frac{\bar{\chi}^H_{zz,+1}(k_0\cos(\theta))}{H^{(2)}_1(k_0r_0\sin(\theta))} \cong -\frac{i\pi k_0 r_0\sin(\theta)}{2\left\{2\ln\left[\gamma k_0 r_0\sin(\theta)x/2\right] + i(\pi - B)\right\}}\left[1/\tilde{x}_1^2 + iD\right], \tag{22}$$

where $\tilde{x}_1$ and D are given in Appendix A. Finally,

$$E_\varphi(R, \varphi = 0, \theta) \cong \\ \frac{1}{\pi^2}\frac{e^{-ik_0R}}{R}\frac{i\pi k_0 r_0}{2\left\{2\ln\left[\gamma k_0 r_0\sin(\theta)x/2\right] + i(\pi - B)\right\}}\left[1/\tilde{x}_1^2 + iD\right] j^e_{1,\varphi}(\theta). \tag{23}$$

4. FORMULATION OF THE ELECTRIC DIPOLE PROBLEM AND FAR FIELD EVALUATION, OR GOUBAU LINE EXCITATION WITH A TANGENTIAL ELECTRIC DIPOLE

In order to check and analyze the CMA far field new features, which will be discussed later, take up the complementary problem about the Goubau line [24] excitation with an electric dipole. The structure to consider is a circular dielectric substrate surrounding a circular metal cylinder and carrying inside the electric dipole

$$\mathbf{J}^e(r, z, \varphi) = \mathbf{r}_p\frac{I^e_0 L}{r}\delta(r - r_p)\delta(z - z_p)\delta(\varphi - \varphi_p) \tag{24}$$

where

$$\mathbf{r}_P = \cos(\beta)\mathbf{i}_Z + \sin(\beta)\mathbf{i}_\varphi. \tag{24a}$$

Here $\mathbf{i}_Z$ and $\mathbf{i}_\varphi$ are the unit vectors along the z- and φ-axes, β is the angle between the current vector and the z-axis, r_P, z_p, φ_p are the dipole coordinates (the coordinate system of Fig. 1), L is the dipole length, $\mathbf{r}_p$ is the vector specifying the dipole current direction. As seen from (24a), vector $\mathbf{r}_p$ is tangential to the surface $r = const$. Upon the Inverse Fourier Transform, the z-components of the field produced by dipole current (24) at the $r = r_0$ interface are

$$\{E_z(r_0,\varphi,z), H_z(r_0,\varphi,z)\} = \sum_{n=-\infty}^{\infty} \int_{h=-\infty}^{\infty} \{e_{nz}(r_0,h), h_{nz}(r_0,h)\} e^{-ih(z-z_p)} e^{-in(\varphi-\varphi_p)} dh, \quad (25)$$

where $e_{n\,z}(r_0,h)$ and $h_{n\,z}(r_0,h)$ are the unknown spectral quantities.

To start the finding of $e_{n\,z}(r_0,h)$ and $h_{n\,z}(r_0,h)$ refer to the expressions [27] of the z-components of the electric and magnetic fields caused in an infinite dielectric medium by current (24):

$$E_z^I(r,\varphi,z) = \sum_{n=-\infty}^{\infty} e^{-i\cdot n\cdot(\varphi-\varphi_p)} \int_{h=-\infty}^{\infty} dh e^{-i\cdot h\cdot(z-z_p)} \frac{C_0}{r_0} f_0 \left\{ \begin{array}{ll} J_n(\tilde{k}_\varepsilon r_P) H_n^{(2)}\left(\tilde{k}_\varepsilon r\right) & r > r_P \\ H_n^{(2)}(\tilde{k}_\varepsilon r_P) J_n\left(\tilde{k}_\varepsilon r\right) & r < r_P \end{array} \right\}, \quad (26)$$

$$H_z^I(r,\varphi,z) = \sum_{n=-\infty}^{\infty} e^{-i\cdot n\cdot(\varphi-\varphi_p)} \int_{h=-\infty}^{\infty} dh e^{-i\cdot h\cdot(z-z_p)} \frac{C_0}{r_0} \Phi_0 \left\{ \begin{array}{ll} J_n'\left(\tilde{k}_\varepsilon r_P\right) H_n^{(2)}\left(\tilde{k}_\varepsilon r\right) & r > r_P \\ H_n^{(2)'}\left(\tilde{k}_\varepsilon r_P\right) J_n\left(\tilde{k}_\varepsilon r\right) & r < r_P \end{array} \right\}, \quad (27)$$

$$f_0 = \frac{x_1^2 \cos(\beta) W_0}{ik_0 r_0 \varepsilon_r} + \frac{inh \sin(\beta) W_0}{\varepsilon_r (r/r_0)}, \quad \Phi_0 = -x_1 \sin(\beta),$$

$$d_n^-(\xi,r) = H_n^{(2)}(\xi) J_n(\tilde{k}_\varepsilon r), \quad d_n^+(\xi,r) = J_n(\xi) H_n^{(2)}(\tilde{k}_\varepsilon r),$$

$$\xi = \tilde{k}_\varepsilon r_P, \quad x_1 = \tilde{k}_\varepsilon^2 r_0 = r_0 \sqrt{k_0^2 \varepsilon_r - (h/k_0)^2}, \quad C_0 = \frac{I_0^e L}{8\pi i}.$$

When the Goubau line is excited with current (24), the field in the homogeneous partial domains $j = 0$, 1 is sought as the excitation plus

the scattered fields in the interior $r_1 < r < r_0\,(j = 1)$ domain and as the scattered field — in the exterior $r > r_0\,(j = 0)$ one:

$$E_z(r,\varphi,z) = \begin{cases} E_z^I(r,\varphi,z) + E_{z1}^S(r,\varphi,z) & r_1 < r < r_0 \\ E_{z0}^S(r,\varphi,z) & r > r_0 \end{cases}, \tag{28}$$

$$H_z(r,\varphi,z) = \begin{cases} H_z^I(r,\varphi,z) + H_{z1}^S(r,\varphi,z) & r_1 < r < r_0 \\ H_{z0}^S(r,\varphi,z) & r > r_0 \end{cases}. \tag{29}$$

The scattered field will be sought in the form

$$\begin{Bmatrix} E_{z1}^S(r,\varphi,z) \\ E_{z0}^S(r,\varphi,z) \end{Bmatrix} = \sum_{n=-\infty}^{\infty} e^{-i\cdot n\cdot(\varphi-\varphi_p)} \int_{h=-\infty}^{\infty} dh e^{-i\cdot h\cdot(z-z_p)} \frac{C_0}{r_0} \begin{cases} A_{1n}^E H_n^{(2)}\left(\tilde{k}_1 r\right) + B_{1n}^E J_n\left(\tilde{k}_1 r\right) & r_1 < r > r_0 \\ A_{02n}^E H_n^{(2)}\left(\tilde{k}_0 r\right) & r > r_0 \end{cases} \tag{30}$$

$$\begin{Bmatrix} H_{z1}^S(r,\varphi,z) \\ H_{z0}^S(r,\varphi,z) \end{Bmatrix} = \sum_{n=-\infty}^{\infty} e^{-i\cdot n\cdot(\varphi-\varphi_p)} \int_{h=-\infty}^{\infty} dh e^{-i\cdot h\cdot(z-z_p)} \frac{C_0}{r_0} \begin{cases} A_{1n}^H H_n^{(2)}\left(\tilde{k}_1 r\right) + B_{1n}^H J_n(\tilde{k}_1 r) & r_1 < r > r_0 \\ A_{0n}^H H_n^{(2)}\left(\tilde{k}_0 r\right) & r > r_0 \end{cases}, \tag{31}$$

where $A_{0,1n}^{E,H}$ and $B_{1n}^{E,H}$ are the unknown coefficients coming from the meeting of the boundary conditions that the tangential components of the total electric field (E_z, E_φ) vanish on the metal cylinder surface and the tangential components of the total electric and magnetic fields (E_z, E_φ, H_z, H_φ) are continuous across the dielectric-air interface $r = r_0$. The result is the algebraic equation system

$$\begin{cases} A_{0n}^E H_n^{(2)}(x_0)\bar{\Delta}_n + A_{0n}^H H_n^{(2)}(x_0) W_0 \Delta_n^H = \Phi_{on}\tilde{d}_n^H \\ A_{0n}^E H_n^{(2)}(x_0)\Delta_n^E + A_{0n}^H H_n^{(2)}(x_0) W_0 \bar{\Delta}_n = f_{on}\tilde{d}_n^E \end{cases} \tag{32}$$

whose solution is

$$A_{0n}^E(h) H_n^{(2)}(x_0) = \frac{\Delta_{1n}(h)}{\Delta_n(h)}, \quad A_{0n}^H(h) H_n^{(2)}(x_0) = \frac{\Delta_{2n}(h)}{\Delta_n(h)},$$

where

$$\Delta_{1n}(h) = \Phi_0 \tilde{d}_n^H(r_P)\bar{\Delta}_n - f_0 \tilde{d}_n^E(r_P)\Delta_n^H,$$
$$\Delta_{n2}(h) = f_0 \tilde{d}_n^E(r_P)\bar{\Delta}_n - \Phi_0 \tilde{d}_n^H(r_P)\Delta_n^E,$$

$$\tilde{d}_n^H(r_P) = \left(\frac{2\mu_r W_0}{\pi x_1^2}\right) \frac{\left[d_{n\xi z}^{+''}(\xi,\bar{x}_1) - d_{n\xi z}^{-''}(\xi,\bar{x}_1)\right]}{\left[J_n'(x_1)H_n^{(2)'}(\bar{x}_1) - H_n^{(2)}(\bar{x}_1)J_n'(x_1)\right]},$$
$$\tilde{d}_n^E(r_P) = \left(-\frac{2\varepsilon_r}{\pi x_1^2}\right) \frac{[d_n^+(\xi,\bar{x}_1) - d_n^-(\xi,\bar{x}_1)]}{\left[J_n(x_1)H_n^{(2)}(\bar{x}_1) - H_n^{(2)}(\bar{x}_1)J_n(x_1)\right]}.$$

Finally the z-components of the field in the open exterior domain are

$$E_{z0}^S(r,\varphi,z) = \frac{C_0}{r_0}\sum_{n=-\infty}^{\infty} e^{-i\cdot n\cdot(\varphi-\varphi_p)} \int_{h=-\infty}^{\infty} dh e^{-ih(z-z_p)} A_{0n}^E H_n^{(2)}\left(\tilde{k}_0 r\right),$$
$$H_{z0}^S(r,\varphi,z) = \frac{C_0}{r_0}\sum_{n=-\infty}^{\infty} e^{-i\cdot n\cdot(\varphi-\varphi_p)} \int_{h=-\infty}^{\infty} dh e^{-ih(z-z_p)} A_{0n}^H H_n^{(2)}\left(\tilde{k}_0 r\right). \tag{33}$$

The asymptotical representation [25] of far-field Fourier integrals (33) with the connection formulas of the far-field spherical wave components yield

$$E_\theta^S(R,\theta,\varphi) = -\frac{1}{\sin\theta}\frac{C_0}{r_0}\frac{e^{-i\,k_0 R}}{R}\Phi^E(\theta,\varphi), \tag{34a}$$
$$E_\varphi^S(R,\theta,\varphi) = \frac{W_0}{\sin\theta}\frac{C_0}{r_0}\frac{e^{-i\,k_0 R}}{R}\Phi^H(\theta,\varphi), \tag{34b}$$

where

$$\Phi^E(\theta,\varphi) = 2\sum_{n=-\infty}^{\infty} e^{ik_0\cos\theta z_p} e^{-in(\varphi-\varphi_0)} i^{n+1} A_{0n}^E(k_0\cos\theta),$$
$$\Phi^H(\theta,\varphi) = 2\sum_{n=-\infty}^{\infty} e^{ik_0\cos\theta z_p} e^{-in(\varphi-\varphi_0)} i^{n+1} A_{0n}^H(k_0\cos\theta).$$

Notice that the obtained formulas are valid for any tangential dipole orientation. The situation $\beta = 0^\circ$ (see (24a)) corresponds to the z-oriented dipole and $\beta = 90^\circ$ — to the φ-oriented dipole. Hence, the electric dipole far field will be calculated by formulas (34).

In addition, the electric dipole and the CMA results will be compared using a complementary case of the dipole location at the medium interface $r_P = r_0$. Then $\xi = x_1$, and the $\tilde{d}_n^H(r_P)$ and $\tilde{d}_n^E(r_P)$ expressions become

$$\tilde{d}_n^H(r_P) = \left(\frac{2\mu_r W_0}{\pi x_1^2}\right) \frac{\left[J_n'(\xi)H_n^{(2)'}(\bar{x}_1) - H_n^{(2)'}(\xi)J_n'(\bar{x}_1)\right]}{\left[J_n'(x_1)H_n^{(2)'}(\bar{x}_1) - H_n^{(2)}(\bar{x}_1)J_n'(x_1)\right]} = \left(\frac{2\mu_r W_0}{\pi x_1^2}\right)\left(\frac{\gamma_{1n}^{H'}(r_0)}{\gamma_{1n}^{H}(r_0)}\right), \tag{35}$$

$$\tilde{d}_n^E(r_P) = \left(-\frac{2\varepsilon_r}{\pi x_1^2}\right) \frac{\left[J_n(x_1)H_n^{(2)}(\bar{x}_1) - H_n^{(2)}(x_1)J_n(\bar{x}_1)\right]}{\left[J_n(x_1)H_n^{(2)}(\bar{x}_1) - H_n^{(2)}(\bar{x}_1)J_n(x_1)\right]} = \left(-\frac{2\varepsilon_r}{\pi x_1^2}\right). \tag{36}$$

In this case, the solution of system (32) is

$$A_{0n}^E(h)H_n^{(2)}(x_0) = \cos(\beta)\left[-\frac{2i}{\pi}\bar{\chi}_{zzn}^E(h)\right] + \sin(\beta)\left[\frac{2i}{\pi}\bar{\chi}_{z\varphi n}^E(h)\right], \tag{37}$$

$$A_{0n}^H(h)H_n^{(2)}(x_0) = \cos(\beta)\left[\frac{2i}{\pi}\bar{\chi}_{zzn}^H(h)\right] + \sin(\beta)\left[\frac{2i}{\pi}\bar{\chi}_{z\varphi n}^H(h)\right]. \tag{38}$$

If the sheet current distribution on the CMA patch is transformed to the delta source

$$\mathbf{j}^{e,dip}(r_0, z', \varphi') = \frac{I_0^e L}{r_0}\left[\cos(\beta)\mathbf{i}_Z + \sin(\beta)\mathbf{i}_\varphi\right]\delta\left(z' - z_P\right)\delta\left(\varphi' - \varphi_P\right) \tag{39}$$

and (39) is substituted into the CMA field expression (8), the result will coincide with that issuing from the dipole location at the $r = r_0$ interface according to (34a) with (37)–(38) substituted.

5. DISCUSSION OF THE RESULTS, COMPARISON OF CMA AND ELECTRIC DIPOLE RADIATION PATTERNS IN ELECTRICALLY SMALL CYLINDER CASE

Consider the characteristic features of the CMA far field towards a comparative analysis of the CMA and the electric dipole. Let us

start with the z-polarized patch case (θ-polarized wave excitation), the probe is symmetric about the φ axis, $\varphi_p = 0$. The co-polar pattern in the E-plane (E_θ versus θ) is presented in Fig. 3 for the CMA with the z-polarized patch and for the z-oriented electric dipole ($\beta = 0°$). The calculations correspond to different frequencies: $f = 1.3\,\text{GHz}$ (curve 1), 1.7 GHz (curve 2), and 2.2 GHz (curve 3); the CMA has the same geometrical and constitutive parameters as in [17]. The solid line presents the rigorous calculation by (8), (10), the crosses show the approximate calculation by (17), and the triangles make up the radiation pattern of the z-oriented electric dipole ($\beta = 0°$) according to formula (34a).

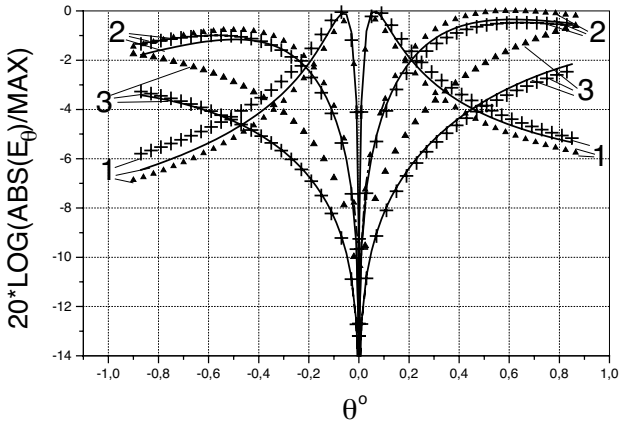

Figure 3. The co-polar pattern in the E-plane (E_θ versus θ) for the CMA with the z-polarized patch and for the z-oriented electric dipole ($\beta = 0°$) at different frequencies: $f = 1.3\,\text{GHz}$ (curve 1), 1.7 GHz (curve 2), and 2.2 GHz (curve 3). The solid line plots the rigorous calculations by formula (12), the crosses come from approximate formula (17), the triangles show the radiation pattern of the z-oriented electric dipole (formula 34a).

The function $E_\theta(R, \varphi = 0, \theta)$ versus θ demonstrates a very good agreement between the numerical calculation results from small-θ approximation formula (17) and the rigorous calculation in terms of the full-wave Fourier analysis of the CMA. Also Fig. 3 demonstrates that the far field behavior of the CMA and the electric dipole is the same for small θ angles.

For the lowest frequency in Fig. 3 $E_\theta(\theta)$ shows local maxima at $\theta = \pm 0.18°$ (curve 1). It has been numerically found that as either frequency or cylinder radius decreases, the maximum grows sharp and shifts towards the cylinder. As the frequency increases (curves 2 and

3), the maximum goes away from the cylinder and gradually dies. The far field pattern therewith smoothes out at small θ angles. So, upon Fig. 3, the $E_\theta(\theta)$ local maximum at a small θ is readily apparent only when the cylinder is electrically small.

Thus, the examination of the $E_\theta(R, \varphi = 0, \theta)$dependence at a small θ can adopt formula (17), which owes to the spectral Green's function peculiarities at $n = 1$. Formula (17) shows that function $E_\theta(R, \varphi = 0, \theta)$decreases like $O(1/\ln(\theta))$ as $\theta \to 0$.

Physically the obtained result is explained by that the field is substantially concentrated nearby the cylinder of a small wave size. Similarly to a planar microstrip antenna, the spherical wave field decreases, sooner or later, as the observation point nears the dielectric substrate surface, for the medium interface, either planar or cylindrical, does not maintain spherical waves.

Notice that the limiting point $\theta = 0^\circ$ is beyond the present spherical wave consideration. And the reported data hold true for any small θ but for zero, as does the scenario of the far field decrease. The point $\theta = 0^\circ$ gets inside the metal rod in the cylindrical coordinate system chosen, and considering the $\theta = 0^\circ$ case serves no purpose. Yet of interest is the far field behavior on the dielectric substrate surface. This field is due to the surface waves not decaying with the z-distance from the source and, also, due to the branch point contribution (case $h/k_0 = 1$ in (5)). It is known that in the small θ case, the radiation pattern can demonstrate an extra lobe when, at the given frequency, the surface wave of the Goubau line becomes a leaking one. However, in our case of a small wave size CMA, only fundamental waves with no cut-off frequency are supported, and we are far off the leaking mode frequency of some high-order wave of the Goubau line [22, 24].

Now proceed to the φ-polarized patch case (φ-polarized wave excitation), the probe is symmetric about the z-axis so that $z_p = 0$. Approximate formula (23) was numerically validated for the far-field E_φ calculation at a small θ angle. See Fig. 4 for the co-polar pattern in the H-plane (E_φ versus θ) at different frequencies $f = 1.1\,\text{GHz}$ (curve 1), $1.2\,\text{GHz}$ (curve 2), $1.4\,\text{GHz}$ (curve 3), and $1.6\,\text{GHz}$ (curve 4). The solid line plots the rigorous calculation results from (10) and (18). The crosses are for the approximate results from (23). The triangles display the far field of the φ-oriented electric dipole ($\beta = 90^\circ$) calculated by (34b). A very good agreement between the rigorous and approximate (by formula (23)) calculations is evident. Besides, the far field of the electric dipole behaves the same as the CMA field in the small θ case. At the lowest considered frequency $f = 1.1\,\text{GHz}$, $E\varphi(\theta)$ runs pronounced maxima at $\theta = \pm 0.0079^\circ$. As in θ-polarization case, the maximum moves away from the cylinder and gradually disappears

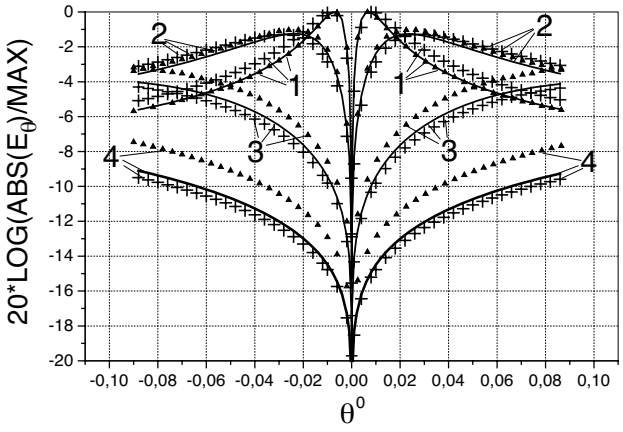

Figure 4. The co-polar pattern in the H-plane (E_φ versus θ) for the CMA with the φ-polarized patch and for the φ-oriented electric dipole ($\beta = 90^\circ$) at different frequencies: $f = 1.1$ GHz (curve 1), 1.2 GHz (curve 2), 1.4 GHz (curve 3), and 1.6 GHz (curve 4). The solid line plots rigorous calculations from formulas (10), (18). The crosses come from approximate formula (23), the triangles show the radiation pattern of the φ-oriented electric dipole.

as frequency rises. From (23) it follows that as θ decreases, the E_φ-component does the same as $O(1/\ln(\theta))$. The physical features of the spherical wave behavior near the interface in the φ-polarization case are similar to those in θ polarization (see 2.1).

The results from 2.1 and 2.2 suggest the following conclusion. The main contributor to the spherical wave field in the far zone at a small θ is the $n = 1$ harmonic of Fourier series for θ-polarization (12) and φ-polarization (18). The situation is similar to the Goubau line excitation by the annular electric current with the azimuthal wave traveling

$$\mathbf{J}^{e,circle}(r', z', \varphi') = I_0 \left[\cos(\beta)\mathbf{i}_Z + \sin(\beta)\mathbf{i}_\varphi\right] \delta(z' - z_P)\delta(r' - r_0)e^{-i\varphi'}. \tag{40}$$

Annular current (40) circulates on the dielectric substrate $r = r_0$. The current phase changes per circle from 0 to 2π according to (40). Notice that only the $n = 1$ harmonic of Fourier series (12) and (18) is retained when current distribution (40) is substituted into (9). So, it is the source of (40) type that provides the dependences observed in Figs. 3 and 4 at $\beta = 0^\circ$ and 90°, respectively.

Turn back to the situation when the patch current distribution is transformed to the electric dipole current given by (39). From (24a) it

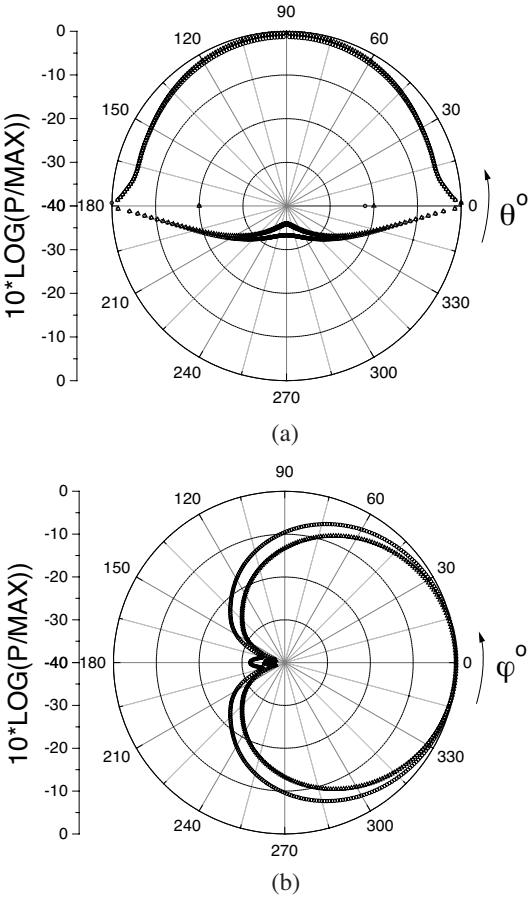

Figure 5. The power pattern in the E-plane (a) and in the H-plane (b) for the CMA with the z-polarized patch (triangles) and for the z-oriented electric dipole (circles).

follows that $\beta = 0^\circ$ corresponds to the z-oriented dipole, and $\beta = 90^\circ$ — to the φ-oriented dipole. Substituting (39) into (9) yields

$$\begin{aligned} \mathbf{j}_n^{e,dip}(\theta) &= j_{nz}^{e,dip}(\theta)\mathbf{i}_Z + j_{n\varphi}^{e,dip}\mathbf{i}_\varphi \\ &= I_0 L\left[\cos(\beta)\mathbf{i}_Z + \sin(\beta)\mathbf{i}_\varphi\right] e^{in\varphi_P} e^{ik_0\cos(\theta)z_P}, \end{aligned} \tag{41}$$

indicating that the spectral density of the dipole current is a constant dependent on the dipole orientation provided that θ is small.

As has been already shown, any conclusion about the spherical wave field components of an electrically small CMA at a small θ is

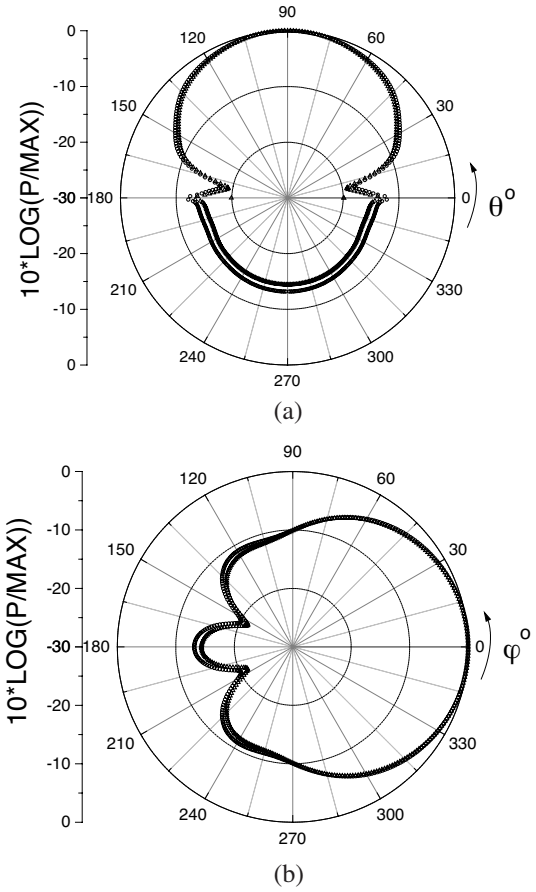

Figure 6. The power pattern in the H-plane (a) and in the E-plane (b) for the CMA with the φ-polarized patch (triangles) and for the φ-oriented electric dipole (circles).

immediately true for the field components of an electric dipole placed on a dielectric substrate. This is because $j^e_{n\,s}(\theta)$ of the CMA little depends on θ, provided that θ is small (see (9)). Therefore $j^e_{1,z}(\theta)$ in (17) and $j^e_{1,\varphi}(\theta)$ in (23) can be taken as constants, as in the electric dipole case. So, the CMA small-θ approximation formulas and diagrams hold true for an electric dipole with $j^{e,dip}_{1,s}(\theta)$ instead of $j^e_{1,s}(\theta)$. In this case, the z- and φ-oriented dipoles are equivalent to the CMA with the z- and φ-polarized patches, respectively.

Furthermore, the far field of an electrically small CMA is similar to

the electric dipole field not only at a small θ and $\varphi = 90^\circ$ but any θ and φ as well. Figs. 5 and 6 display the radiation pattern computations in spherical-wave power terms for the z- and φ-oriented dipoles (circles) and for the CMA with the z- and φ-polarized patches (triangles). The radiation pattern in power terms comes from the formula

$$P = -\frac{R^2}{2\sin^2\theta}\left[w_0\left|H_z\right|^2 + \frac{1}{w_0}\left|E_z\right|^2\right]. \tag{42}$$

The structure parameters are as in [14]. Namely, the patch size is $W_z = 0.03\,\mathrm{m}$ and $W_\varphi = 0.04\,\mathrm{m}$, $\varepsilon_r = 2.32$, $r_1 = 0.1\,\mathrm{m}$, the substrate thickness is $d = 0.0795\,\mathrm{cm}$. According to [14], the resonant frequencies in z- and φ-polarization cases are, respectively, $f = 3.28$ and $2.46\,\mathrm{GHz}$. When the radiation pattern is considered in power terms, the features of $P(\theta)$ behavior at a small θ come from the results obtained for the field components in Section 3. Namely, $P(\theta)$ runs like $O(1/\ln^2(\theta))$ as the angle tends to zero. A comparison of the dipole and the CMA radiation patterns in power terms in Figs. 5 and 6 confirms that they bear strong resemblance, physical and numerical. This keeps true until $r_0/\lambda_0 < 0.5$. All similarity ends, first quantitatively then qualitatively, as r_0/λ_0 increases. And the finite size of the patch enhances the effect on the radiation pattern.

It has been shown that the CMA radiation pattern in the case of a small wave size and a thin substrate can be evaluated in the approximation of an electric dipole on the Goubau line surface. In thin substrate case, resonant frequencies are found by the approximate analytical formula from [14].

6. CONCLUSION

The far field of a small wave size CMA has been analyzed, with specific features of the spherical wave field components recognized. Namely, for the z- and φ-polarized patches, the co-polar pattern local maxima have been found for an electrically small CMA in the small elevation angle case. Also it has been shown that a similar maximum occurs in the far field of an electric dipole taken instead of the patch. It has been demonstrated that this maximum is due to the annular electric current radiation with $n = 1$ azimuthally traveling wave harmonic, which corresponds to the $n = 1$ harmonic of the electric dipole field series expansion. As the CMA electric size increases, the local maximum gradually disappears. Approximate analytical expressions for the θ- and φ-components of the spherical wave field have been obtained, describing the effect. In the small elevation angle case, a very good

agreement has been demonstrated between the rigorously calculated and analytically evaluated far field of the CMA and the rigorously calculated far field of the electric dipole. The reported data not only account for the familiar run of the characteristics but also reveal some yet unknown far field features depending on the elevation angle when the latter is small.

It has been shown that the radiation pattern of a small wave size CMA bears strong resemblance to the pattern of an electric dipole placed on the Goubau line surface in θ and φ polarizations over a wide range of θ and φ angles.

APPENDIX A.

Field components (1)–(2) in terms of the current spectral density are derived through the meeting of the boundary condition across the air-dielectric interface carrying the equivalent surface electric current and also on the metal cylinder [23]. The resulting spectral Green's function is

$$\chi_{pqn}^{E,H}(r,h) = \bar{\chi}_{pqn}^{E,H}(h)\gamma_{n0}(r,h) = \bar{\chi}_{pqn}^{E,H}(h)\left[H_n^{(2)}\left(r\tilde{k}_0\right)/H_n^{(2)}(x_0)\right], \tag{A1}$$

$$\bar{\chi}_{zzn}^{E}(h) = -\frac{\Delta_n^H w_0}{\Delta_n k_0 r_0},\ \bar{\chi}_{z\varphi n}^{E}(h) = \frac{in\bar{h}}{x_1 x_0}\left[\frac{\gamma'_{n0}(r_0,h)}{x_1\bar{\gamma}_{n0}(r_0,h)} - \frac{\bar{\gamma}'_{n1}(r_0,h)}{x_0\bar{\gamma}_{n1}(r_0,h)}\right]\frac{w_0}{\Delta_n}, \tag{A2}$$

$$\bar{\chi}_{zzn}^{H}(h) = \frac{\bar{\Delta}_n w_0}{\Delta_n k_0 r_0}, \quad \bar{\chi}_{z\varphi n}^{H}(h) = -\frac{n\bar{h}\bar{\Delta}_n}{x_1^2\Delta_n} - \frac{i}{x_1}\frac{\bar{\gamma}'_{n1}(r_0,h)}{\bar{\gamma}_{n1}(r_0,h)}\frac{\Delta_n^E}{\Delta_n}, \tag{A3}$$

where

$$\bar{\Delta}_n = n\bar{h}\left[x_1^{-2} - x_0^{-2}\right], \quad \Delta_n^E = -i\left[\Phi_n - \varepsilon_r F_n\right], \quad \Delta_n^H = i\left[\Phi_n - \bar{F}_n\right] \tag{A4}$$

$$\Phi_n = \frac{\gamma'_{n0}(r_0,h)}{x_0\gamma_{n0}(r_0,h)}, \quad F_n = \frac{\gamma'_{n1}(r_0,h)}{x_1\gamma_{n1}(r_0,h)}, \quad \bar{F}_n = \frac{\bar{\gamma}'_{n1}(r_0,h)}{x_1\bar{\gamma}_{n1}(r_0,h)}, \tag{A5}$$

$$\Delta_n(h) = \bar{\Delta}_n(h) - \Delta_n^E(h)\cdot\Delta_n^H(h), \quad \gamma_{n0}(r,h) = \frac{H_n^{(2)}(\tilde{k}_0 r)}{H_n^{(2)}(\tilde{k}_0 r_0)}, \tag{A6}$$

$$\{\gamma_{n1}(r,h), \bar{\gamma}_{n1}(r,h)\} = \frac{H_n^{(2)}\left(\tilde{k}_1 r\right)}{H_n^{(2)}\left(\tilde{k}_1 r_1\right)} + \left\{\Gamma_1\frac{J_n(\tilde{k}_1 r)}{J_n\left(\tilde{k}_1 r_1\right)}, \bar{\Gamma}_1\frac{J_n(\tilde{k}_1 r)}{J_n\left(\tilde{k}_1 r_1\right)}\right\}, \tag{A7}$$

$$\Gamma_1 = -\frac{J_n(\bar{x}_1)H_n^{(2)}(x_1)}{J_n(x_1)H_n^{(2)}(\bar{x}_1)}\cdot, \quad \overline{\Gamma}_1 = -\frac{J'_n(\bar{x}_1)H_n^{(2)}(x_1)}{J_n(x_1)H'^{(2)}_n(\bar{x}_1)}, \tag{A8}$$

$$\tilde{k}_i^2 = k_0^2\left\{\varepsilon_{ri}\mu_{ri} - \overline{h}^2\right\}, \quad x_0^2 = r_0^2\tilde{k}_0^2, \quad x_1^2 = r_0^2\tilde{k}_1^2, \quad \bar{x}_1^2 = r_1^2\tilde{k}_i^2, \tag{A9}$$

$$\varepsilon_{ri} = \begin{cases} \varepsilon_{r1} = \varepsilon_r & r_1 < r < r_0 \\ \varepsilon_{r0} = 1 & r_1 > r_0 \end{cases}, \quad \overline{h} = h/k_0 \tag{A10}$$

where $J_n(x)$ is the Bessel function and $H_n^{(2)}(x)$ is the Hankel function of the second kind. The derivation of (17) and (23) was made by introducing the constants

$$B = \frac{i\gamma'_{n1}\left(r_0, \bar{h}=1\right)}{\tilde{x}_1\gamma_{n1}\left(r_0, \bar{h}=1\right)}, \quad D = -\frac{i\,\bar{\gamma}'_{n1}\left(r_0, \bar{h}=1\right)}{\tilde{x}_1\bar{\gamma}_{n1}\left(r_0, \bar{h}=1\right)}, \tag{A11}$$

where $\tilde{x}_1 = k_0 r_0\sqrt{\varepsilon_r - 1}$.

ACKNOWLEDGMENT

The author would like to thank V. Volski and V. Kryzhanovskiy for the valuable comments and fruitful discussions.

REFERENCES

1. Acar, R. C. and G. Dural, "Mutual coupling of printed elements on a cylindrically layered structure using closed-form Green's function," *Progress In Electromagnetics Research*, PIER 78, 103–127, 2008.
2. Liano, S.-L. and R. J. Vernon, "On the image approximation for electromagnetic wave propagation and PEC scattering in cylindrical harmonics," *Progress In Electromagnetics Research*, PIER 66, 65–88, 2006.
3. Angiulli, G., G. Amendola, and G. D. Massa, "Radiation from dielectric coated elliptic conducting cylinder by assigned electric current distribution," *Progress In Electromagnetics Research*, PIER 57, 131–150, 2006.
4. Shooshtari, A. and A. R. Sebak, "Electromagnetic scattering by parallel metamaterial cylinders," *Progress In Electromagnetics Research*, PIER 57, 165–177, 2006.
5. Hill, S. C. and J. M. Jarem, "Scattering of multilayer concentric elliptical cylinders excited by single mode source," *Progress In Electromagnetics Research*, PIER 55, 209–226, 2005.

6. Toyama, H. and K. Yasumoto, "Electromagnetic scattering from periodic arrays of composite circular cylinder with internal cylindrical scatterers," *Progress In Electromagnetics Research*, PIER 52, 321–323, 2005.
7. Hamid, A.-K., "Axially slotted antenna on a circular or elliptic cylinder coated with metamaterials," *Progress In Electromagnetics Research*, PIER 51, 329–341, 2005.
8. Hamid, A.-K., "Multi-dielectric loaded axially slotted antenna on circular or elliptic cylinder," *Journal of Electromagnetic Waves and Applications*, Vol. 20, No. 9, 1259–1271, 2006.
9. Najjar-Khatirkolaei, B., M. Al-Kanhal, and A. R. Sebak, "Electromagnetic wave scattering by elliptic chiral cylinder," *Journal of Electromagnetic Waves and Applications*, Vol. 20, No. 10, 1377–1390, 2006.
10. Ruppin, R., "Scattering of electromagnetic radiation by perfect electromagnetic conductor cylinder," *Journal of Electromagnetic Waves and Applications*, Vol. 20, No. 13, 1853–1860, 2006.
11. Acar, R. C. and G. Dural, "Comments on 'A complete set of spatial domain dyadic Green's function components for cylindrically stratified media in fast computational form'," *Journal of Electromagnetic Waves and Applications*, Vol. 18, No. 10, 1389–1394, 2004.
12. Krowne, C. M., "Cylindrical-rectangular microstrip antenna," *IEEE Trans. Antennas Propagation*, Vol. 31, 194–199, 1983.
13. Wu, K. Y. and J. F. Kaufman, "Radiation pattern computation for cylindrical-rectangular microstrip antenna," *IEEE Antennas Propagation Soc. Int. Symp. Dig.*, 39–43, 1983.
14. Luk, K.-M., K.-F. Lee, and J. S. Dahele, "Analysis of the cylindrical-rectanular patch antenna," *IEEE Trans. Antennas and Propagation*, Vol. 37, No. 2, 143–147, 1989.
15. Nakatani, N. and N. G. Alexopoulos, "Accurate Green's function computation for printed circuit antennas on cylindrical substrates," *Electromagnetics*, Vol. 6, 243–254, 1986.
16. Silva, F. C., S. B. A. Fonseca, A. J. M. Soares, and A. J. Giarola, "Analysis of microstrip antennas on circular-cylindrical substrates with a dielectric overlay," *IEEE Trans. Antennas and Propagation*, Vol. 39, No. 9, 1398–1404, 1991.
17. Habashy, T. M, S. M. Ali, and J. A. Kong, "Input impedance and radiation pattern of cylindrical-rectangular and wraparound microstrip antennas," *IEEE Trans. Antennas and Propagation*, Vol. 38, No. 6, 722–731, 1990.

18. Svezhentsev, A. Y. and G. A. E. Vandenbosch, "Efficient spatial domain moment method solution of cylindrically rectangular microstrip antennas," *IEE Proceedings, Microwaves, Antennas and Propagation*, Vol. 153, Issue 4, 376–384, August 2006.
19. He, M. and X. Xu, "Full-wave analysis and wide-band design of probe-fed multilayered cylindrical-rectangular microstrip antennas," *IEEE Trans. Antennas and Propagation*, Vol. 52, No. 7, 1749–1757, 2004.
20. Erturk, V. B. and R. G. Rojas, "Efficient analysis of input impedance and mutual coupling of microstrip antennas mounted on large coated cylinders," *IEEE Trans. Antennas and Propagation*, Vol. 51, No. 4, 739–749, 2003.
21. Raffaeli, S., Z. Sipus, and P.-S. Kildal, "Analysis and measurements of conformal patch array antennas on multilayer circular cylinder," *IEEE Trans. Antennas and Propagation*, Vol. 53, No. 3, 1105–1113, 2005.
22. Svezhentsev, A. Y. and G. A. E. Vandenbosch, "Mixed-potential Green's functions for sheet electric current over metal-dielectric cylindrical structure," *Journal of Electromagnetic Waves and Application*, Vol. 16, No. 6, 813–835, 2002.
23. Svezhentsev, A. Y. and G. A. E. Vandenbosch, "Spatial Green's function singularity for sheet electric current over dielectric coated cylinder," *IEEE Trans. on Antenna and Propagation*, Vol. 52, No. 2, 608–610, 2004.
24. Goubau, G., "Surface waves and their applications transmission lines," *J. Appl. Phys.*, Vol. 21, No. 11, 1119–1128, 1950.
25. Harrington, R. F., *Time-Harmonic Electromagnetic Fields*, 245, McGraw-Hill Book Company, 1961.
26. Abramowitz, M. and I. A. Stegun, *Handbook of Mathematical Functions*, Dover, New York, 1971.
27. Markov, G. T. and A. F. Chaplin, *Electromagnetic Wave Excitation*, Radio i Svyaz', Moscow, 1983 (in Russian).